

Electronic, magnetic, and optical properties of bulk and (111)-surfaces of CoMnZnSi quaternary Heusler alloy

Ramesh Paudel^{1,*}, Jing-Chuan Zhu², Moaid K. Hussain³, Mohammed Batouche⁴,
Muhammad Waqas Qureshi², Durga Paudyal^{5,6,7}

¹Nepal Academy of Science and Technology, Khumaltar, Lalitpur 44700, Nepal

²School of Materials Science and Engineering, Harbin Institute of Technology, Harbin 150001, China

³AL-Hussain University College, Karbala, Iraq

⁴Laboratoire de Physique Quantique et de Modélisation Mathématique, Université de Mascara, Mascara 29000, Algeria

⁵Ames Laboratory, Iowa State University, Ames, IA 50011-3020, USA

⁶Electrical and Computer Engineering Department, Iowa State University, Ames, IA 50011, USA

⁷Computer Science Department, Iowa State University, Ames, IA 50011, USA

*Corresponding author: Email: r.paudel@hit.edu.cn

Abstract

The structural stability, electronic structure, and magnetic and optical properties of CoMnZnSi quaternary Heusler alloy (QHA) in the bulk and (111)-slab forms have been investigated by performing density functional theory (DFT) calculations. Formation and cohesive energies, and elastic constants confirm that the bulk CoMnZnSi is chemically and mechanically stable at an equilibrium lattice parameter of 5.81 Å. The calculated elastic constants also indicate that this QHA has ductile and anisotropic features. We investigate and discuss the bonding behavior from charge density distribution and density of states. These calculations in the bulk phase show a perfect half-metallic behavior with an integer value of magnetic moment (4 μ_B) and a large spin-flip gap of 0.39 eV. On the other hand, the Co (111) and Si (111)-slabs exhibit semi-metallic nature at the Fermi level. These results indicate that CoMnZnSi qualifies for spintronic applications. In the bulk and Co (111), Zn (111), and Si (111)-surfaces, the magnetic moment of Co and Mn atoms are ferromagnetically aligned, while the ferrimagnetic alignment of Co with Mn has been found in Mn (111)-surface. We also investigate the optimal conductivity, dielectric functions, reflectivity, absorption coefficient, refractive index, and loss function to understand the underlying optical properties of this alloy.

Keywords: Heusler alloy; Phase stability; Electronic structure; Magnetic nature; Spintronic

1. Introduction

Magneto-electronic (spintronic) devices have drawn a considerable attention as future generation electronics[1]. These spintronic devices make use of both spin and charge degrees of freedom in which a highly effective spin source is vital. Half-metallic Heusler alloys are one of the most suitable spin sources owing to high spin-polarization arising from an energy gap for one spin channel[2]. Some quaternary Heusler alloys (QHAs), the so-called Y-type, have 100% spin-polarization with half-metallicity and with Curie temperature higher than the room temperature, which are essential for spin-dependent devices. The Co-based QHAs are among the most commonly explored (theoretically and experimentally), including CoFeMnSi for magnetic tunnel junctions[3], CoFeMnZ (Z = Si, As, Sb)[4] for physical properties, CoFeCrX (X = Si, Ge)[5] and CoFeZrZ (Z = Ge, Sb, Si)[6] for magnetic and electronic structure, and CoFeHfGe[7] for bulk and surface properties.

The element-specific magnetic moments and spin-resolved density of states (DOS) of CoFeMnZ (Z = Al, Ga, Si, Ge) alloys have been measured using circular dichroism in X-ray-absorption spectroscopy[8] and correlated with *ab initio* results. The CoMnCrZ (Z = Al, Si, Ge, As)[9] QHAs have been investigated for their chemical and mechanical stabilities using generalized gradient approximation (GGA)-based exchange-correlation functionals. These compounds are half-metallic ferromagnets, in particular CoMnCrAs has the most significant bandgap of 1.14 eV and half-metallic gap of 0.50 eV. The electronic structure, magnetism, mechanical and thermoelectric properties of the CoXMnAs (X = Ru, Rh)[10] QHAs have been investigated using GGA, modified Becke-Johnson (mBJ), and GGA+U approaches. Nevertheless, for CoXMnAs, GGA and mBJ **did not predict a half-metallic behavior**; however, GGA+U depicted a half-metallic character in the spin-down channel. The elastic constants confirmed structural stability with ductile nature and, the alteration of the Seebeck coefficient and electronic conductivity signified the half-metallic behavior. The half-metallic and magnetic properties of the CoFeZrSi[11] alloy with tetragonal and triclinic distorted primitive cell was studied using first-principles. The CoFeZrSi alloy possesses half-metallic characteristics when the primitive cell is tetragonally distorted, whereas the half-metallicity disappears when the unit cell is triclinically deformed.

The electronic and magnetic properties for the (001) and (111)-surfaces of YCoCrGe[12] QHA have been investigated from first-principles. The half-metallicity with 100% spin-polarization was found in bulk and destroyed in surfaces except for the Cr (111)-slab. The magnetic moment for bulk composition is found to be an integer value. The (111), (110), and (001) surfaces of QHA CoRuMnSi[13] were computed by density functional theory (DFT). These calculations showed half-metallic nature for the Si-terminated (111) surface while the half-metallicity preserved in the bulk CoRuMnSi which is destroyed at Co, Ru, and Mn-(111) surfaces. The surface states destroyed the band gap in the spin-down channel at both MnSi- and CoRu-terminated (001)-surfaces, while a nearly half-metallicity is found for the (110)-surfaces.

These previous theoretical and experimental studies motivated us to investigate the phase stability, half-metallicity, and magnetism in the bulk as well as (111)-surfaces of CoMnZnSi. In addition, mechanical and optical properties of bulk CoMnZnSi have been investigated. Here, we have systematically studied the half-metallicity and magnetism of these materials using DFT based on GGA exchange-correlation functional. The results show that the half-metallicity is retained in the bulk form, while semi-metallic nature is revealed in Co (111) and Si (111)-surfaces.

2. Computational details

Here, we have employed DFT based plane-wave pseudopotential method implemented in Cambridge Serial Total Energy Package (CASTEP)[14,15]. There are several approximations that have been developed, namely, the local density approximation (LDA), GGA, meta-GGA, and hybrid functionals. Each of these approximations conveys different definitions and approaches and is suitable for specific materials. Among them, the LDA and GGA are the ones widely used in DFT calculations of QHAs. The extension to improve the accuracy of LDA is provided by the second approximation known as GGA. This formalism uses two variables instead of one variable as in LDA (the electron density): the electron density and its gradient, as given by the equation: $E_{XC}^{GGA}[n(r)] = \int n(r)e_{XC}^{hom}[n(r), \nabla n(r)]dr$. Besides, several corrected functionals are developed in GGA formalism to include different contributions from the exchange and correlation part. These functionals are Perdew, Burke, and Ernzerhof (PBE); Perdew, Burke, and Ernzerhof for solid (PBEsol)[16]; and Perdew-Wang 1991 (PW91). We have used widely recognized PBE[17]. The reciprocal space was sampled by a mesh of $12 \times 12 \times 12$ k-points in the Brillouin zone, and the cut-off energy of 450 eV was fixed for all measures after numerous tests. In these tests, the cut-off energy was set from 300 to 600 eV at the interval of 20 eV, and k-points were set from $4 \times 4 \times 4$ to $15 \times 15 \times 15$ with $1 \times 1 \times 1$ interval. The ground state structural properties were investigated using Broyden-Fletcher-Goldfarb-Shanno (BFGS)[18] technique, while the convergence tolerance were set as follows: total energy tolerance = 5×10^{-6} eV/atom, stress component = 0.02 GPa, maximum force = 0.01 eV/Å, and the maximum displacement of an atom during the geometry optimization = 0.0005 Å. The surface layers were constructed by cleaving the optimized bulk structure of CoMnZnSi along the (111) planes; a vacuum space of 10 Å is inserted along the z-direction. A mesh of $12 \times 12 \times 1$ k-points was used in the Brillouin zone for all slabs. The energetically favorable (111) surface was considered as also indicated in the literature[19,20]. Furthermore, the optical properties have been calculated using a complex dielectric function relation[21].

3. Results and discussion

3.1 Stability: structural and mechanical

The compound CoMnZnSi retains LiMgPdSn[22] or Y-type QHA with the space group of $F\bar{4}3m$ (Fig. 1a). In Y-type structure, there are four interpenetrating face-centered cubic sub-lattices with atomic positions: Co (0, 0, 0), Mn (0.25, 0.25, 0.25), Zn (0.5, 0.5,

0.5), and Si (0.75, 0.75, 0.75). We performed energy minimization as a function of lattice constant within ferromagnetic (FM, or spin-polarized) and nonmagnetic (NM, or non-spin-polarized) configurations to obtain the accurate ground state (Fig. 1b). The total energy with FM configuration is lower (equilibrium lattice parameter of 5.81 Å) than that of the NM configuration, which suggests that the FM configuration is more stable than the NM configuration. The properties with the FM configuration are therefore discussed below.

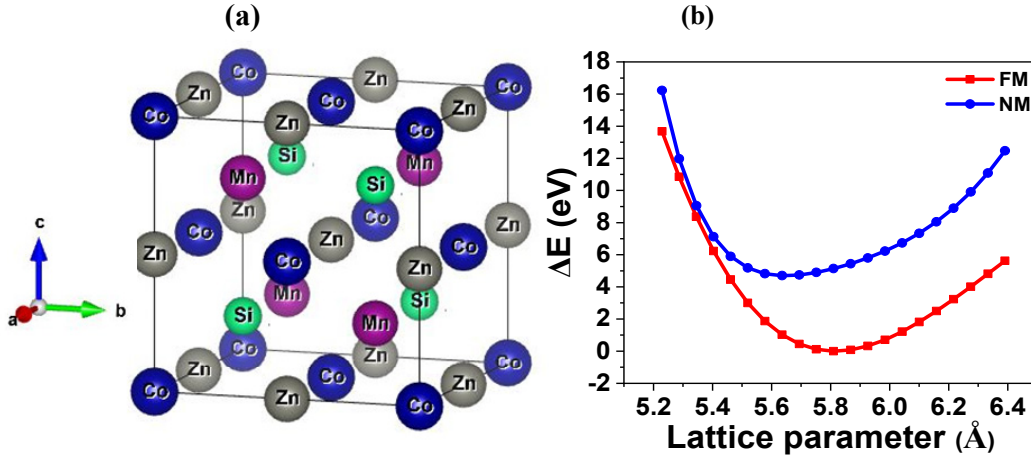


Fig. 1. (a) Crystal structure of CoMnZnSi and (b) energy difference as a function of lattice parameter for FM and NM configurations.

Table 1. Lattice parameter a (Å), cohesive energy $E_C^{CoMnZnSi}$, formation energy $E_f^{CoMnZnSi}$.

| Alloy | a (Å) | Ref. a (Å) | $E_C^{CoMnZnSi}$ | $E_f^{CoMnZnSi}$ |
|----------|---------|-----------------|------------------|------------------|
| CoMnZnSi | 5.81 | 5.81 [23] | -2.85 | -0.27 |

To find and understand the structural stability of CoMnZnSi, we have calculated and analysed formation and cohesive energies, and elastic constants. We note that there is no experimental structural data available for this compound. The formation energy, E_f , is computed using the formula:

$$E_f^{CoMnZnSi} = E_{tot}^{CoMnZnSi} - (E_{Co}^{bulk} + E_{Mn}^{bulk} + E_{Zn}^{bulk} + E_{Si}^{bulk}), \quad (1)$$

where $E_{tot}^{CoMnZnSi}$ is the equilibrium total energy per unit formula for CoMnZnSi alloy; E_{Co}^{bulk} , E_{Mn}^{bulk} , E_{Zn}^{bulk} and E_{Si}^{bulk} relates to the total energy per atom for the Co (HCP), Mn (BCC), Zn (HCP), Si (FCC), respectively. The computed formation energy of -0.27 eV/atom indicates the chemical stability from the point of view of enthalpy, and could be synthesized experimentally. Also, the cohesive energy, E_c , is investigated using the following expression:

$$E_c^{CoMnZnSi} = E_{tot}^{CoMnZnSi} - (E_{Co}^{iso} + E_{Mn}^{iso} + E_{Zn}^{iso} + E_{Si}^{iso}), \quad (2)$$

where $E_{tot}^{CoMnZnSi}$ is the total energy per unit formula at optimized state; E_{Co}^{iso} , E_{Mn}^{iso} , E_{Zn}^{iso} , and E_{Si}^{iso} relate to the total energy per isolated atom for Co, Mn, Zn, and Si, respectively. The negative value of E_c (-2.85 eV/atom) confirms the structural stability at the optimized state. The high E_c indicates the difficulty in deforming this alloy due to its strong chemical bond.

Moreover, to check mechanical stability, the elastic constants (C_{ij}) are investigated. The elastic constants are attributed to various underlying solid-state phenomena and are directly connected to thermodynamic properties such as heat capacity, thermal expansion, and Debye temperature. The cubic crystal consists of C_{11} , C_{12} , and C_{44} elastic constants among 21 impartial elastic constants C_{ij} , which are obtained by investigating total energy as a function of volume-preserving strains that break the symmetry. Born and Huang[24] defined the mechanical stability criteria for cubic structure as: $C_{11} > 0, C_{11} - C_{12} > 0, C_{11} + 2C_{12} > 0, C_{44} > 0, C_{11} + C_{12} > 0$. These elastic constants, $C_{11} = 169.38$ GPa, $C_{12} = 134.38$ GPa, and $C_{44} = 86.50$ GPa show that this alloy is mechanically stable at the optimized state.

Table 2 Calculated elastic constants C_{11} , C_{12} , and C_{44} (GPa), bulk modulus B (GPa), shear modulus G, Young's modulus E, and Poisson's ratio ν .

| Compound | C_{11} | C_{12} | C_{44} | B_V | B_R | B_H | G_R | G_V | G_H | E | ν | B/G |
|----------|----------|----------|----------|--------|--------|--------|-------|-------|-------|--------|-------|------|
| CoMnZnSi | 169.38 | 134.38 | 86.50 | 146.05 | 146.05 | 146.05 | 58.90 | 33.56 | 46.23 | 125.46 | 0.35 | 3.15 |

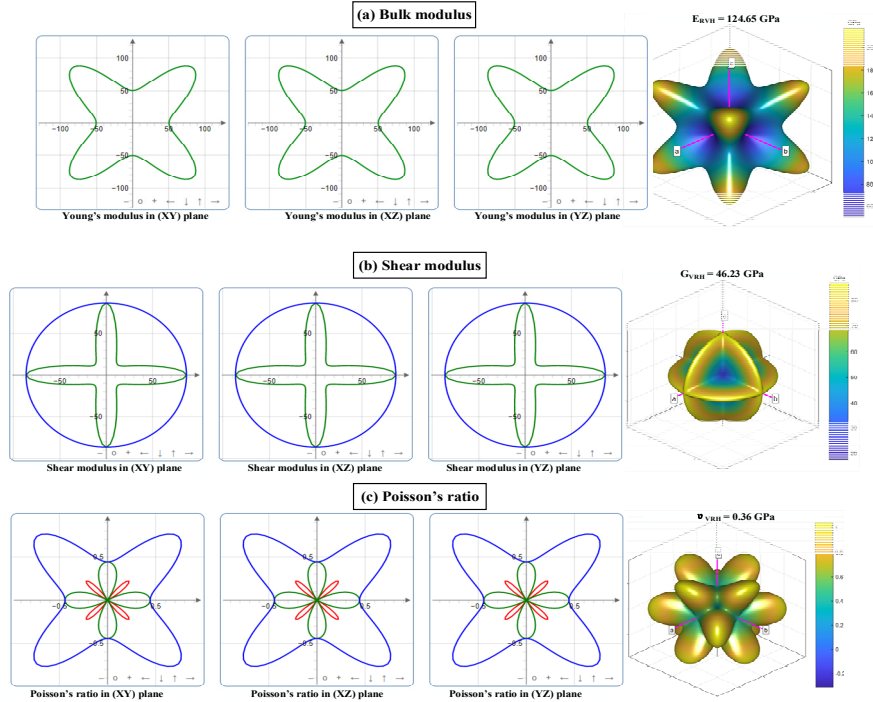


Fig. 2. Directional dependent 2D projections and 3D plots of Young's modulus (a), Shear modulus (b), and Poisson's ratio (c).

It is known that the mechanical properties of anisotropic materials are direction-dependent, which means that the properties are not identical in all crystallographic planes. Therefore, mechanical anisotropy is an essential factor that helps to understand the anisotropic deformation of materials. The open-source software packages AnisoVis and ELATE are used to visualize the anisotropic behavior in 2 dimensional (2D) and 3 dimensional (3D) of Young's and shear moduli, and Poisson's ratio in different crystal planes[25]. Figure 2a shows the 2D projections and 3D plots of Young's modulus (Y). It is noticed that Young's modulus exhibits anisotropic nature in all crystallographic planes, which can be seen from the non-circular 2D projections. For isotropic materials, the 2D projections (3D plots) are perfectly circular (spherical). The anisotropic nature of Young's modulus can also be seen from the 3D plot. In 2D projections, the minimum values of Y are at around 45° of the horizontal and vertical axis in all planes.

Figure 2(b) shows the anisotropic behavior of shear modulus (G), which consists of two surfaces. The blue (green) line in 2D projections represent the maximum (minimum) values of G in a particular crystallographic plane. The 2D projections of outer surface (blue lines) of G are circular and have maximum values at the horizontal and vertical axis in all planes, while the inner surface (green lines) exhibits the maximum values at the horizontal and vertical axis and minimum values are at around 45° of the vertical and horizontal axis. The 3D plots of G gives better visualization of anisotropy. Similarly, the anisotropy of Poisson's ratio (ν) is demonstrated in Fig. 2(c). The 2D projections of ν consist of three surfaces (outer-middle-inner) which are represented by the blue-green-red lines. The Poisson's ratio also shows similar behavior as that of shear modulus. The 3D plot exhibits different colors which are associated with maximum and minimum values of ν .

3.2. Electronic and magnetic properties

a) Bulk

The electronic structure at the Fermi level shows half-metallic band gap. Due to the hybridization of $3d$ states of Co and Mn, a gap in the minority spin channel emerges. Figure 3 shows the predicted spin-polarized band structure and density of states (DOS). The band structure is investigated along the $W - L - G - X - W - K$ high symmetry direction. The majority channel shows metallic character whereas minority channel indicate a band gap at the Fermi level (Fig. 3a). The indirect band gap of 0.27 eV (Table 3) is found in the spin-down (minority) channel. The valence band maximum (VBM) and conduction band minimum (CBM) are at the L and X points of the Brillouin zone. The half-metallic (spin-flip) gap, which is the minimum energy required to flip a minority-spin electron from the valence band maximum to the Fermi level, is of 0.39 eV (Table 3). The results revealed that CoMnZnSi is a true half-metallic ferromagnet.

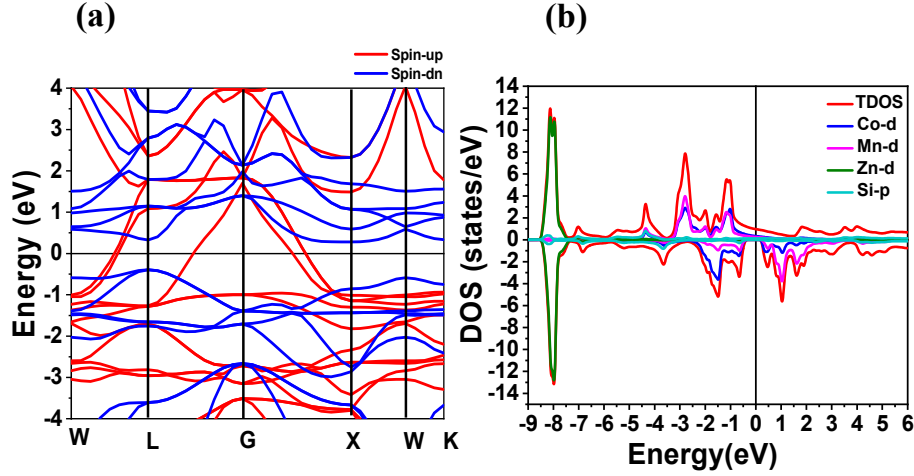


Fig. 3. (a) Bulk band structure, (b) total and partial density of states.

To further understand the characteristic of electronic structure, the total density of states (DOS) and atom-projected DOS have been analyzed. Figure 3b represents the spin-polarized total DOS and atom-projected DOS in the ground state structure. The total DOS shows the metallic nature for majority spin channel and semiconducting or insulating nature in the minority spin channel. The band gap in the minority spin is mainly due to the splitting of bonding t_{2g} and antibonding t_{1u} coming from Co and Mn (Fig. 3b). *Zn-3d states contribute below -7.39 eV with negligible effect on the magnetic moments and half-metallicity.* A similar mechanism of band gap formation due to the hybridization of $3d-3d$ orbitals has been found in other quaternary Heusler compounds[9,26–28]. The spin-polarization, $P = [(D\uparrow - D\downarrow)/(D\uparrow + D\downarrow)]$, calculations revealed that the CoMnZnSi is a true half-metallic compound with 100% spin-polarization.

Table 3 shows the ground state total and atom projected magnetic moments. The perfect half-metallic Heusler alloys have the integer total magnetic moment per formula unit and obey Slater-Pauling rule[29–32]($M_T = N_v - 18$) μ_B , where N_v is the total number of valence electrons/formula unit. The result indicates that CoMnZnSi is a ferromagnet with a total magnetic moment of 4 μ_B /f.u. Here the Mn atom contributes the most of the magnetic moment. The magnetic moments of Co and Mn are positive (Table 3) exhibiting the existence of ferromagnetic coupling. However, Zn and Si with negative magnetic moments reveal their antiferromagnetic coupling with Co and Mn.

Table 3 Total and atom projected magnetic moments, band gap and half-metallic (spin-flip) gap.

| Alloy | μ_{Co} | μ_{Mn} | μ_{Zn} | μ_{Si} | μ_{Total} | E_{bg} | E_{HM} |
|----------|------------|------------|------------|------------|---------------|----------|----------|
| CoMnZnSi | 0.64 | 3.55 | -0.09 | -0.10 | 4.00 | 0.66 | 0.39 |

To elucidate the bonding nature, we study the charge density distribution along the (110) crystallographic plane (Fig. 4). The charge accumulation and deficiency is

represented by red and yellowish-green color, respectively. These colors indicate ionic and covalent characteristics, respectively. The overlap of charges between Co and Mn is larger than Mn and Zn due to the stronger hybridization between Co-3*d* and Mn-3*d* (Fig. 3b). The spherical shape of charge accumulation in Co, Mn, and Zn results in a strong covalent bond, which allows CoMnZnSi to be a stable structure. This is an agreement with other quaternary Heusler alloys such as NiCuMnZ (Z = In, Sn, and Sb)[27].

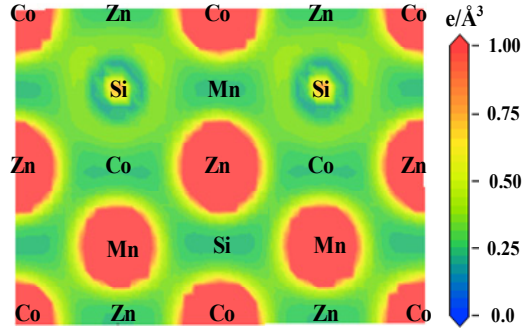


Fig. 4. Charge density distribution map in the (110) plane. Charge density distribution spans from 0 to $1 e/\text{\AA}^3$. 0 and 1 represent metallic and covalent bonding respectively. The yellowish-green color represents ionic bonding.

b) Surface

To examine half-metallicity and spin-polarization in thin-film form of CoMnZnSi, we investigate (111) terminated surface electronic structure. Figure 5 shows majority and minority spin band structure of Co (111), Mn (111), Zn (111) and Si (111) surfaces. The Fermi level has a metallic intersection in both minority and majority spin channels, indicating the destruction of half-metallicity. The computed total DOS for Co (111), Mn (111), Zn (111), and Si (111) surfaces are shown in Fig. 7. The Co (111) and Si (111)-slabs indicate the semi-metallic behavior with spin-polarization of 80.3% and 90.8%, while Mn (111) and Zn (111) indicate metallic characteristics with spin-polarization of 31.7% and 10.9%, respectively.

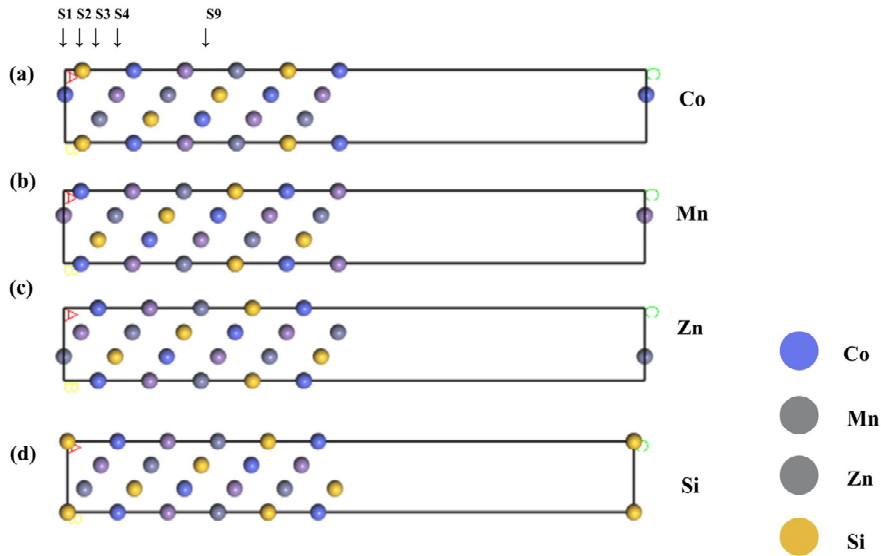


Fig. 5. Surface layers of a) Co (111), b) Mn (111)-surface, c) Zn (111), and Si (111). A, B, and C represent the axes.

The atom projected magnetic moments (APMM) for Co (111), Mn (111), Zn (111), and Si (111)-surfaces in the layer 1 (S1), layer 2 (S2), layer 3 (S3), layer 4 (S4), and layer 9 (S9) are shown in Fig. 8. For the Co (111)-surface, Mn (S4) shows the highest magnetic moment ($3.35 \mu_B$), which is very similar to the bulk APMM. The Co atom shows the ferromagnetic interaction with other atoms in S1 and S9, while Zn and Si show the ferrimagnetic interaction in S2 and S3. For the Mn (111)-surface, the APMM of the Mn atom increases as we move from S1 to S9 but the Co atom shows negative magnetic moments indicating ferrimagnetic interaction between other atoms in S3. The Mn (S4) also shows the highest magnetic moment ($4.05 \mu_B$) in the Zn (111)-surface, while Zn in S9 is nearly equal to the corresponding atom with the bulk counterpart.

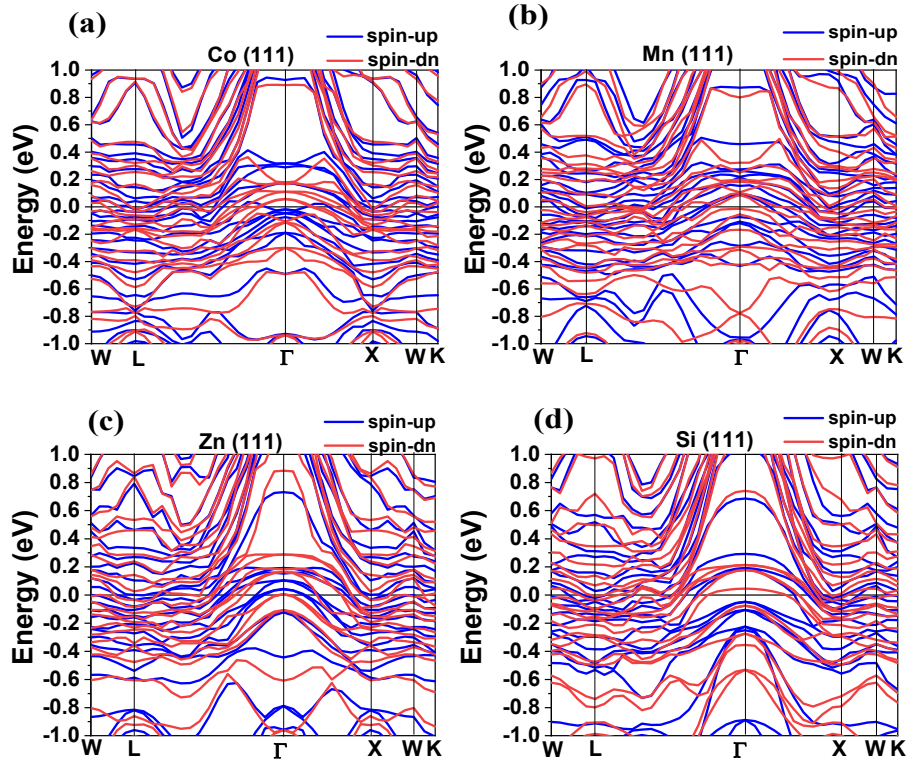


Fig. 6. Surface majority and minority band structure with (a) Co (111), (b) Mn (111), (c) Zn (111), and (d) Si (111) terminations.

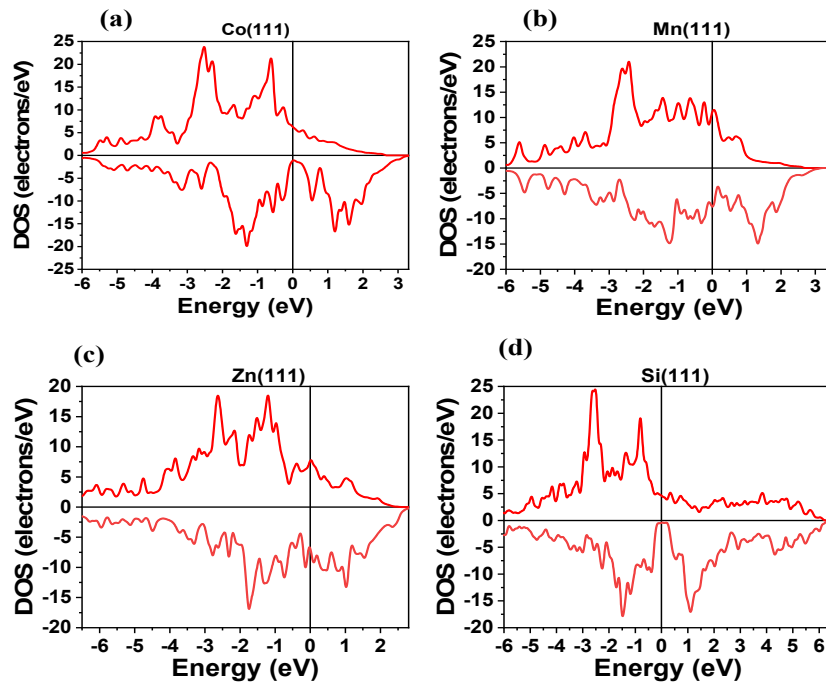


Fig. 7. Surface density of states with (a) Co (111), (b) Mn (111), (c) Zn (111), and (d) Si (111) terminations.

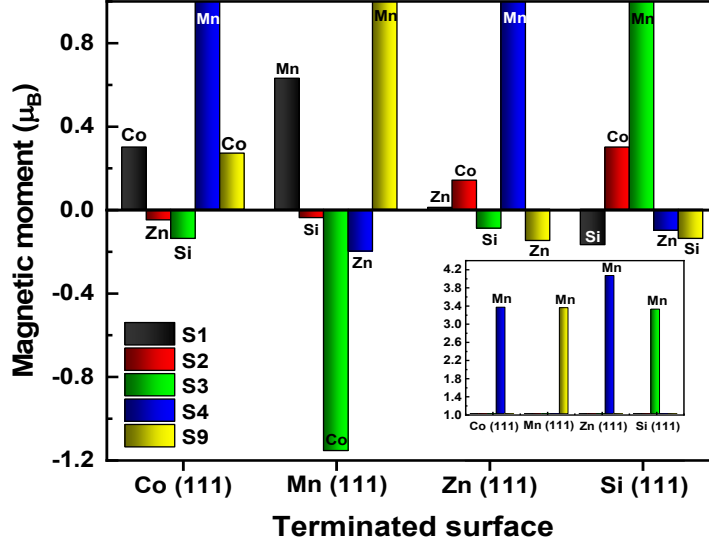


Fig. 8. Atom projected magnetic moments (APMM, μ_B) of (111)-surface terminations.

3.3 Optical characteristics

The optical properties are determined by the complex frequency-dependent dielectric function $\varepsilon(\omega) = \varepsilon_1(\omega) + i\varepsilon_2(\omega)$. Here $\varepsilon_1(\omega)$ and $\varepsilon_2(\omega)$ are real and imaginary part of the dielectric function, respectively. We use the following equations to calculate the imaginary and real part of dielectric functions.

$$\varepsilon_2 = \frac{4\pi e^2}{m^2 \omega} \int d^k \sum_{n,n'} |\langle kn | p | kn' \rangle|^2 \times f_{kn} (1 - f_{kn'}) \delta(E_{kn} - E_{kn'} - \hbar\omega) \quad (6)$$

$$\varepsilon_1(\omega) = 1 + \frac{2}{\pi} M \int_0^\infty \frac{\omega' \varepsilon_2(\omega')}{\omega'^2 - \omega^2} d\omega' \quad (7)$$

Once the complex dielectric function is known, then all other properties, i.e., optical conductivity (σ), reflectivity (R), energy loss (L), absorption coefficient (I), and refractive index (n) can be derived. These properties within photon energy up to 30 eV are shown in Fig. 9. The real part of $\varepsilon_1(\omega)$ and imaginary part of $\varepsilon_2(\omega)$ of dielectric functions with incident photon energy is shown in Fig. 9(a). The dielectric function's real part $\varepsilon_1(\omega)$ corresponds to the permeability component that measures the energy stored in the material. The imaginary part $\varepsilon_2(\omega)$ is associated with the energy loss of the optical system into the medium. The $\varepsilon_2(\omega)$ approaches to zero from above at around 25 eV and $\varepsilon_1(\omega)$ gets to zero

from below at approximately 19.7 eV. The trend of $\epsilon_1(\omega)$ and $\epsilon_2(\omega)$ of dielectric function while approaching zero represents the metallic nature. Moreover, $\epsilon_2(\omega)$ has its maximum value within the IR region and becomes zero in the UV region.

Refractive index $n(\omega)$ is one of the optical constants calculated by:[33]

$$n(\omega) = \sqrt{\frac{\epsilon_1 + \sqrt{(\epsilon_1^2 + \epsilon_2^2)}}{2}} \quad (8)$$

Figure 9b represents the imaginary and real part of the refractive index. The refractive index is 8.20, which decreases with an increase in photon energy. Energy loss function or bulk plasma frequency (ω_p) is defined as the peak, which appears where the imaginary part of dielectric function is less than zero, and the real part of dielectric function is approaching to zero (Fig. 9c). The energy loss function peak is located at ~19.7 eV.

Figure 9d represents conductivity (σ) due to the absorption of photon. The first peak of optical conductivity lies within the visible region, and the highest peak in the UV region, indicating that CoMnZnSi is photoconductive in the visible and UV region. Reasonable value of σ in the visible region also implies that this alloy has a potential for solar cell application[34,35].

Figure 9e represents absorption coefficient (α). The values α increases with an increase in photon energy. The value of the absorption coefficient is weak in the IR region and increases in the visible region with its maximum value in the UV region indicating the high absorbent feature. The maximum value of α is observed at ~6.9 eV. The first significant peak of reflectivity is in the visible region. The highest peak lies in the UV region and approaches to zero at ~31 eV. The reflectivity in the visible region is above 45%. This feature may enable CoMnZnSi to be used as a coating material to minimize solar heating[36–38].

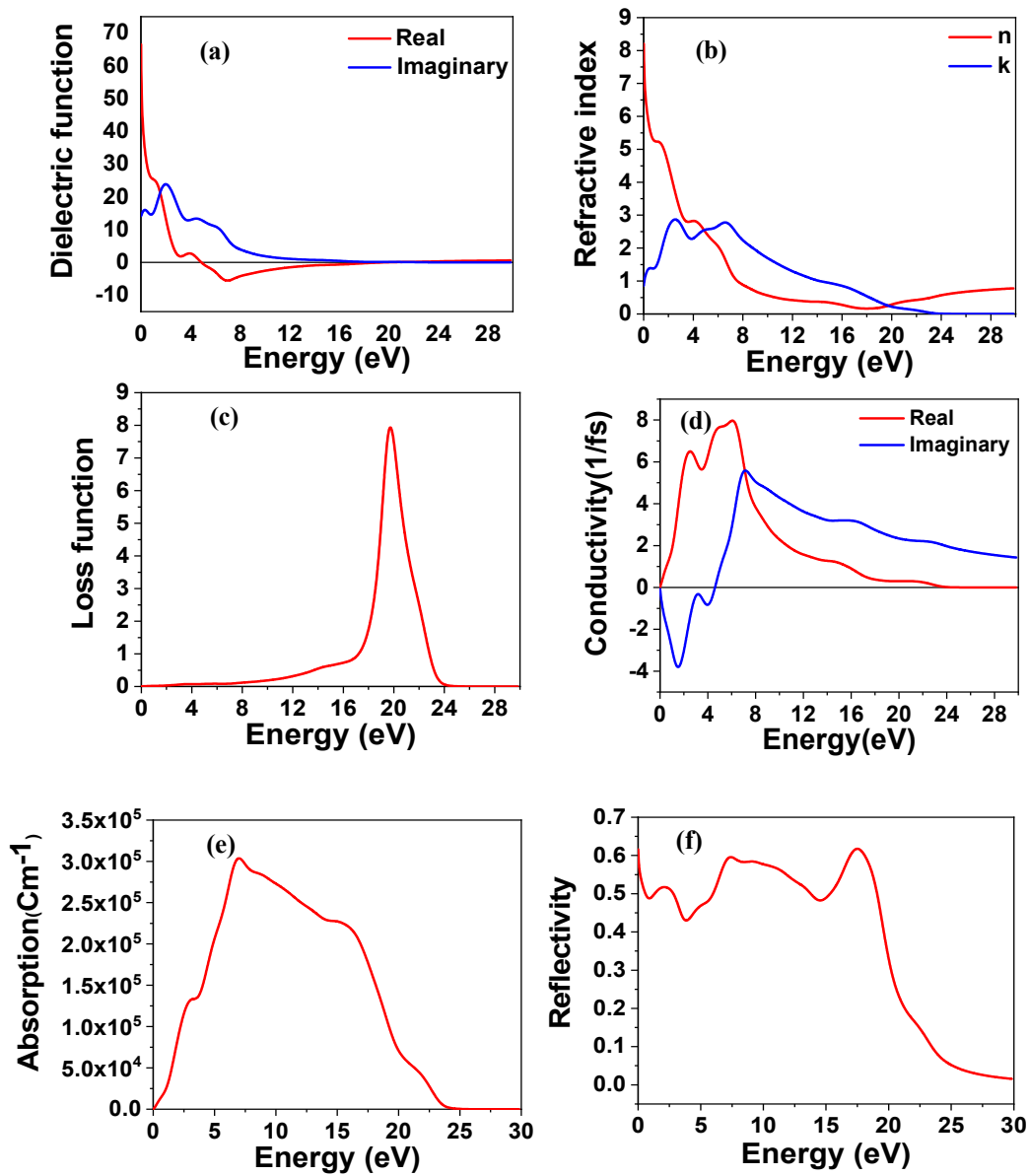


Fig. 9. Optical response as a function of energy. (a) Reflectivity, (b) absorption, (c) refractive index, (d) real and imaginary dielectric function, (e) real and imaginary conductivity and (f) loss function.

4. Conclusion

In summary, phase stability, electronic structure, magnetism, elastic and optical properties of bulk and (111)-surfaces of CoMnZnSi QHA have been systematically studied using DFT. Negative formation and cohesive energies, and elastic properties, confirm that the CoMnZnSi alloy is chemically and mechanically stable. The calculated shear modulus G , bulk modulus B , Young's modulus E , Poisson's and B/G ratios indicate that this alloy in the bulk form is ductile and shows the elastic anisotropic nature. The calculations revealed that the CoMnZnSi is half-metallic, with a band gap of 0.66 eV and with a large spin-flip

gap of 0.39 eV qualifying it for spintronic applications. The band gap is mainly contributed by the Co-3*d* and Mn-3*d* orbitals. The total magnetic moment of 4 μ_B is mainly originated from 3*d* electrons of Co, and the Mn atoms, which satisfies the Slater-Pauling $M_t = Z_t - 24$ rule with 100% spin-polarization. The charge accumulation and depletion in CoMnZnSi reveals the mixture of covalent and ionic bonding within comprising elements. The Co (111) and Si (111)-slabs showed the semi-metallic nature with 80.3 % and 90.8 % spin-polarization, while Mn (111) and Zn (111)-slabs exhibited metallic nature. The Co atom showed that the ferrimagnetic interaction in Mn (111)-surface, which is opposite as compared to the bulk counterpart. The Mn atom mainly contributes to the atomic magnetic moment in all surfaces, which agrees well with the corresponding value in the bulk form. In relation to the optical properties, the absorption coefficient is weaker in the IR region and stronger in the UV region indicating the high absorbent feature and potential application to coating.

Acknowledgement

A part of work done at the Ames Laboratory was conducted for the US-DOE under its contract with Iowa State University, Contract No. DE-AC02-07CH11358.

References

- [1] S.A. Wolf, Spintronics: A Spin-Based Electronics Vision for the Future, *Science*. 294 (2001) 1488–1495. doi:10.1126/science.1065389.
- [2] R.A. De Groot, F.M. Mueller, P.G. Van Engen, K.H.J. Buschow, New class of materials: Half-metallic ferromagnets, *Physical Review Letters*. 50 (1983) 2024–2027.
- [3] S.M. Lakhan Bainsla, Kazuya Z. Suzuki, Masahito Tsujikawa, Hiroki Tsuchiura, Masafumi Shirai, Magnetic tunnel junctions with an equiatomic quaternary CoFeMnSi Heusler alloy electrode, *Applied Physics Letters*. 112 (2018) 052403. doi:10.1063/1.5002763.
- [4] M.H. Elahmar, H. Rached, D. Rached, R. Khenata, G. Murtaza, S. Bin Omran, W.K. Ahmed, Structural, mechanical, electronic and magnetic properties of a new series of quaternary Heusler alloys CoFeMnZ (Z=Si, As, Sb): A first-principle study, *Journal of Magnetism and Magnetic Materials*. 393 (2015) 165–174. doi:10.1016/j.jmmm.2015.05.019.
- [5] Y. Jin, P. Kharel, P. Lukashev, S. Valloppilly, B. Staten, J. Herran, I. Tutic, M. Mitrakumar, B. Bhusal, A. O’Connell, K. Yang, Y. Huh, R. Skomski, D.J. Sellmyer, Magnetism and electronic structure of CoFeCrX (X = Si, Ge) Heusler alloys, *Journal of Applied Physics*. 120 (2016) 053903. doi:10.1063/1.4960350.
- [6] R. Paudel, J. Zhu, Structural, electronic, magnetic, elastic, and thermal properties of Co-based equiatomic quaternary Heusler alloys, *Journal of Magnetism and Magnetic Materials*. 453 (2018) 10–16. doi:10.1016/j.jmmm.2017.12.103.
- [7] R. Paudel, F. Zhou, M. Liao, J. Zhu, Half-metallicity and magnetism of CoFeHfGe novel quaternary Heusler alloy in bulk form as well as (100) and (001) surfaces : An ab initio study, *Journal of Physics and Chemistry of Solids*. 136 (2020) 109190. doi:10.1016/j.jpcs.2019.109190.
- [8] P. Klaer, B. Balke, V. Alijani, J. Winterlik, G.H. Fecher, C. Felser, H.J. Elmers, Element-specific

magnetic moments and spin-resolved density of states in CoFeMnZ (Z=Al, Ga, Si, Ge), *Physical Review B - Condensed Matter and Materials Physics*. 84 (2011) 1–7.
doi:10.1103/PhysRevB.84.144413.

- [9] M.W. Mohamedi, A. Chahed, A. Amar, H. Rozale, A. Lakdja, O. Benhelal, A. Sayede, Ab-initio study of structural, elastic, thermal, electronic and magnetic properties of quaternary Heusler alloys CoMnCrZ (Z = Al, As, Si, Ge), *Eur. Phys. J. B*. 89 (2016) 267. doi:10.1140/epjb/e2016-70183-6.
- [10] A.Q. Seh, D.C. Gupta, Exploration of highly correlated Co-based quaternary Heusler alloys for spintronics and thermoelectric applications, *International Journal of Energy Research*. 43 (2019) 8864–8877. doi:10.1002/er.4853.
- [11] A. Birsan, Small interfacial distortions lead to significant changes of the half-metallic and magnetic properties in Heusler alloys: The case of the new CoFeZrSi compound, *Journal of Alloys and Compounds*. 710 (2017) 393–398.
- [12] M.K. Hussain, K.I. Inad, Theoretical study of surface properties of new (0 0 1)- and (1 1 1)-surface YCoCrGe quaternary Heusler compounds, *Thin Solid Films*. 663 (2018) 100–104.
doi:10.1016/j.tsf.2018.08.017.
- [13] J.M. Khalaf Al-zyadi, A.A. Kadhim, K.-L. Yao, Half-metallicity of the (001), (111) and (110) surfaces of CoRuMnSi and interface half-metallicity of CoRuMnSi/CdS, *RSC Advances*. 8 (2018) 25653–25663. doi:10.1039/C8RA02918K.
- [14] M.D. Segall, P.J.D. Lindan, M.J. Probert, C.J. Pickard, P.J. Hasnip, S.J. Clark, M.C. Payne, First-principles simulation: ideas, illustrations and the CASTEP code, *Journal of Physics: Condensed Matter*. 14 (2002) 2717–2744.
- [15] S.J. Clark, M.D. Segall, C.J. Pickard, P.J. Hasnip, M.I.J. Probert, K. Refson, M.C. Payne, First principles methods using CASTEP, *Zeitschrift Für Kristallographie*. 220 (2005) 567–570.
doi:10.1524/zkri.220.5.567.65075.
- [16] J.P. Perdew, A. Ruzsinszky, G.I. Csonka, O.A. Vydrov, G.E. Scuseria, L.A. Constantin, X. Zhou, K. Burke, Restoring the density-gradient expansion for exchange in solids and surfaces, *Physical Review Letters*. 100 (2008) 1–4. doi:10.1103/PhysRevLett.100.136406.
- [17] J.P. Perdew, K. Burke, M. Ernzerhof, Generalized Gradient Approximation Made Simple, *Physical Review Letters*. 77 (1996) 3865–3868. doi:10.1103/PhysRevLett.77.3865.
- [18] T.H. Fischer, J. Almlöf, General methods for geometry and wave function optimization, *J. Phys. Chem*. 96 (1992) 9768–9774.
- [19] J. Wong, *First-Principles Studies of Surface Energies of Magnetic Full-Heuslers and Machine Learning of Hybrid Perovskites*, University of California, San Diego. (2019) 1–139.
- [20] Y. Li, J. Zhu, R. Paudel, J. Huang, F. Zhou, Ab initio predictions of magnetism and half-metallicity of (111)-surfaces of Co₂CrSi full-Heusler alloy, *Vacuum*. 192 (2021) 110455.
doi:10.1016/j.vacuum.2021.110455.
- [21] D.P. Rai, R.K. Thapa, Study of electronic, magnetic, optical and elastic properties of Cu₂MnAl a gapless full Heusler compound, *Journal of Alloys and Compounds*. 612 (2014) 355–360.
doi:10.1016/j.jallcom.2014.05.056.
- [22] J. Drews, U. Eberz, H.U. Schuster, Optische Untersuchungen an farbigen Intermetallischen Phasen, *Journal of The Less-Common Metals*. 116 (1986) 271–278. doi:10.1016/0022-5088(86)90235-3.
- [23] X. Jia-ling, J. Li-yun, J. Xiao-qing, H. Xing-nan, H. Deng-lu, 系列 CoMnZnZ 四元 Heusler 化合物的, *Acta Physica Sinica*. 68 (2019) 0–7. doi:10.7498/aps.68.20190207.
- [24] M. Born, K. Huang, *Dynamical Theory of Crystal Lattices*, Oxford University Press. (1962) 431.

doi:10.1119/1.1934059.

- [25] J. Nordmann, M. Aßmus, H. Altenbach, Visualising elastic anisotropy: theoretical background and computational implementation, *Continuum Mechanics and Thermodynamics*. 30 (2018) 689–708. doi:10.1007/s00161-018-0635-9.
- [26] X. Wang, Z. Cheng, R. Guo, J. Wang, H. Rozale, L. Wang, Z. Yu, G. Liu, First-principles study of new quaternary Heusler compounds without 3d transition metal elements: ZrRhHfZ (Z = Al, Ga, In), *Materials Chemistry and Physics*. 193 (2017) 99–108. doi:10.1016/j.matchemphys.2017.02.019.
- [27] Y. Ma, H. Hao, Y. Xin, H. Luo, H. Liu, F. Meng, E. Liu, Atomic ordering and magnetic properties of quaternary Heusler alloys NiCuMnZ (Z = In, Sn, Sb), 86 (2017) 121–125. doi:10.1016/j.intermet.2017.03.020.
- [28] M. Rahmoune, A. Chahed, A. Amar, H. Rozale, A. Lakdja, O. Benhelal, A. Sayede, The effect of pressure and alloying on half-metallicity of quaternary Heusler compounds CoMnYZ (Z = Al, Ga, and In), *Materials Science-Poland*. 34 (2016) 905–915. doi:10.1515/msp-2016-0120.
- [29] J.C. Slater, The ferromagnetism of nickel. II. Temperature effects, *Physical Review*. 49 (1936) 931–937.
- [30] L. Pauling, The nature of the interatomic forces in metals, *Physical Review*. 54 (1938) 899–904.
- [31] K. Ozdogan, E. Sasioglu, I. Galanakis, Slater-Pauling behavior in LiMgPdSn-type multifunctional quaternary Heusler materials: Half-metallicity, spin-gapless and magnetic semiconductors, *Journal of Applied Physics*. 113 (2013) 193903.
- [32] I. Galanakis, P.H. Dederichs, N. Papanikolaou, Slater-Pauling behavior and origin of the half-metallicity of the full-Heusler alloys, *Physical Review B*. 66 (2002) 174429. doi:10.1103/PhysRevB.66.174429.
- [33] M. Fox, G.F. Bertsch, *Optical Properties of Solids*, American Journal of Physics. 70 (2002) 1269–1270. doi:10.1119/1.1691372.
- [34] N. Belmiloud, F. Boutaiba, A. Belabbes, M. Ferhat, F. Bechstedt, Half-Heusler compounds with a 1eV (1.7eV) direct band gap, lattice-matched to GaAs (Si), for solar cell application: A first-principles study, *Physica Status Solidi (B) Basic Research*. 253 (2016) 889–894. doi:10.1002/pssb.201552674.
- [35] D. Kieven, R. Klenk, S. Naghavi, C. Felser, T. Gruhn, I-II-V half-Heusler compounds for optoelectronics : Ab initio calculations, (2010) 1–6. doi:10.1103/PhysRevB.81.075208.
- [36] M. Rasheduzzaman, K.M. Hossain, S.K. Mitro, M.A. Hadi, J.K. Modak, M.Z. Hasan, Structural, mechanical, thermal, and optical properties of inverse-Heusler alloys Cr₂CoZ (Z = Al, In): A first-principles investigation, *Physics Letters, Section A: General, Atomic and Solid State Physics*. 385 (2021) 126967. doi:10.1016/j.physleta.2020.126967.
- [37] R. Majumder, S.K. Mitro, B. Bairagi, Influence of metalloid antimony on the physical properties of palladium-based half-Heusler compared to the metallic bismuth: A first-principle study, *Journal of Alloys and Compounds*. 836 (2020) 155395. doi:10.1016/j.jallcom.2020.155395.
- [38] M.W. Qureshi, X. Ma, G. Tang, R. Paudel, Ab initio predictions of structure and physical properties of the Zr₂GaC and Hf₂GaC MAX phases under pressure, *Scientific Reports*. 11 (2021) 1–23. doi:10.1038/s41598-021-82402-1.

